

## Research



**Cite this article:** Kalogirou A, Keaveny EE, Papageorgiou DT. 2015 An in-depth numerical study of the two-dimensional Kuramoto–Sivashinsky equation. *Proc. R. Soc. A* **471**: 20140932. <http://dx.doi.org/10.1098/rspa.2014.0932>

Received: 2 December 2014

Accepted: 1 June 2015

**Subject Areas:**

applied mathematics, computational mathematics, differential equations

**Keywords:**

two-dimensional Kuramoto–Sivashinsky equation, spatio-temporal chaos, equipartition of energy

**Author for correspondence:**

D. T. Papageorgiou

e-mail: [d.papageorgiou@imperial.ac.uk](mailto:d.papageorgiou@imperial.ac.uk)

# An in-depth numerical study of the two-dimensional Kuramoto–Sivashinsky equation

A. Kalogirou, E. E. Keaveny and D. T. Papageorgiou

Department of Mathematics, Imperial College London, London SW7 2AZ, UK

The Kuramoto–Sivashinsky equation in one spatial dimension (1D KSE) is one of the most well-known and well-studied partial differential equations. It exhibits spatio-temporal chaos that emerges through various bifurcations as the domain length increases. There have been several notable analytical studies aimed at understanding how this property extends to the case of two spatial dimensions. In this study, we perform an extensive numerical study of the Kuramoto–Sivashinsky equation (2D KSE) to complement this analytical work. We explore in detail the statistics of chaotic solutions and classify the solutions that arise for domain sizes where the trivial solution is unstable and the long-time dynamics are completely two-dimensional. While we find that many of the features of the 1D KSE, including how the energy scales with system size, carry over to the 2D case, we also note several differences including the various paths to chaos that are not through period doubling.

## 1. Introduction

The one-dimensional Kuramoto–Sivashinsky equation (1D KSE) is

$$u_t + uu_x + u_{xx} + u_{xxx} = 0 \quad (1.1a)$$

and

$$u(x, t) = u(x + 2L, t), \quad u(x, 0) = u_0(x), \quad (1.1b)$$

where  $0 \leq x < 2L$  is the spatial coordinate and  $t$  is time; solutions are sought on spatially periodic domains of size  $2L$ , and  $u_0(x)$  is the initial condition. The KSE is one of the simplest nonlinear PDEs exhibiting complex

spatio-temporal dynamics. It was derived by both Homsy [1] and Nepomnyashchii [2] in their studies of thin liquid film flows down inclined planes, by LaQuey *et al.* [3] in trapped ion mode instabilities, by Kuramoto & Tsuzuki [4] in diffusion-induced chaos in reaction systems, and by Sivashinsky and co-workers [5–7] in their studies of flame front propagation. It has since been found to describe the asymptotic behaviour of other physical phenomena, including two-phase flows in cylindrical pipes [8], interfacial flows [9–11], plasma and chemical reaction dynamics [4,12,13] and models of ion-sputtered surfaces [14] that extend the equation to higher dimensions also. Note that (1.1) is equivalent (in one dimension) to the integrated form

$$v_t + \frac{1}{2}v_x^2 + v_{xx} + v_{xxx} = 0, \quad (1.2)$$

through the transformation  $u = v_x$ . Flame propagation applications are usually governed by the integrated form (1.2), whereas fluid film flows are governed by the conservative form (1.1).

In addition to its intrinsic physical relevance, the 1D KSE has attracted significant mathematical interest, becoming a premier model for studying complex dynamics in spatially extended systems. There have been numerous analytical [15–19] and numerical [20–23] studies of the 1D KSE with  $2L$ -periodic boundary conditions (see below also). The 1D KSE has been proved to possess a unique smooth solution that depends continuously on its initial data [19]. Its convective Burgers-type nonlinearity provides a transfer of energy between active and dissipative modes, and the essence of the dynamics can be captured by a finite-dimensional dynamical system of ODEs for the Fourier coefficients of the solution.

A significant portion of the analytical work on the 1D KSE has focused on how the energy (defined as the  $L_2$ -norm of the solution,  $\|u\|_{L_2} := (\int_0^{2L} u^2(x, t) dx)^{1/2}$ ) scales with domain length. Assuming that the domain is finite ( $L < \infty$ ; if  $L = \infty$  the PDE is ill-posed), long-time solutions are bounded by an absorbing ball with an  $L$ -dependent radius (in  $L_2$  and higher Sobolev spaces) such that

$$\limsup_{t \rightarrow \infty} \|u\|_{L_2} = \mathcal{O}(L^p). \quad (1.3)$$

The first value of  $p$  obtained was  $p = \frac{5}{2}$  for odd-parity solutions [18], though this estimate has been improved over the years by many mathematicians [15,17,24–28]. The current best-known analytic bound is  $\mathcal{O}(L^{3/2})$  [26,28], though the numerical study by Wittenberg & Holmes [29] has suggested the optimal value  $p = \frac{1}{2}$ .

In addition to the energy, there have been several notable studies examining how the solution itself changes with system size. For domain lengths smaller than  $2\pi$ , the 1D KSE is linearly stable and small perturbations from the trivial state will decay exponentially in time. As the domain length increases beyond  $2\pi$ , the trivial solution loses stability to a unimodal steady state, which in turn becomes unstable to multi-modal steady states, travelling waves, oscillatory solutions and finally to chaotic solutions for sufficiently large  $L$ . The transition to chaos occurs through a period doubling cascade that follows the Feigenbaum scenario [22,23,30]. As the solution enters the chaotic regime, it remains of  $\mathcal{O}(1)$ , adding more oscillations as  $L$  increases. It was proved by Kukavica [31] that the number of rapid oscillations of the solution is universally bounded by an expression exponential in  $L$ . This estimate was later improved by Grujić [32] to yield a bound essentially algebraic in  $L$ , though numerical experiments suggest that, as  $L$  increases, the number of oscillations should be  $\mathcal{O}(L)$  [29]. Numerical studies have also shown that the chaotic dynamics are extensive in that the local dynamics are asymptotically independent of  $L$  for  $L \gg 1$  and the energy is equally distributed among the lowest Fourier modes [29].

Despite the rich dynamics established for the 1D KSE, studies in higher dimensions are somewhat limited and primarily analytical. The spatially periodic 2D KSE is

$$u_t + \frac{1}{2}|\nabla u|^2 + \Delta u + \Delta^2 u = 0 \quad (1.4)$$

and

$$u(x, y; t) = u(x + 2L_x, y; t) = u(x, y + 2L_y, t), \quad u(x, y, 0) = u_0(x, y), \quad (1.5)$$

where  $\Delta = \partial_x^2 + \partial_y^2$ . It has been established by Cao & Titi [33] that the only locally integrable stationary solutions of the 2D KSE (on infinite domains) are constant values, but the question of global regularity for the KSE in higher dimensions is still an open problem in nonlinear analysis. The first attempts at proving boundedness, analyticity and stability for the 2D KSE were by Sell & Taboada [34] and Molinet [35]. Assuming a thin domain, Sell & Taboada [34] showed the existence of a bounded absorbing set in  $H_{\text{per}}^1([0, 2\pi] \times [0, 2\pi\epsilon])$  for  $\epsilon$  sufficiently small. Molinet [35] improved this result, showing that with some restrictions on the initial data

$$\limsup_{t \rightarrow \infty} \|u\|_{L_2} \leq \mathcal{O}(L_x^{8/5} L_y^{1/2}), \quad (1.6)$$

on the bounded domain  $(0, 2L_x) \times (0, 2L_y)$  with  $2L_x \geq 2\pi$ ,  $0 < 2L_y < 2\pi$  satisfying

$$\left(1 - \left(\frac{L_y}{2\pi}\right)^2\right)^{-4/9} L_y \leq C L_x^{-67/35}. \quad (1.7)$$

For radially symmetric solutions, Demirkaya & Stanislavova [36] proved that there exists a time-independent bound for the  $L_2$ -norm of the solution, while Michelson [37] showed the existence of a non-trivial radial steady solution that is asymptotically periodic. Other authors have considered variants of the 2D KSE, mostly taking the form

$$u_t + \frac{1}{2}(u_x^2 + \alpha u_y^2) + (u_{xx} + \beta u_{yy}) + \Delta^2 u = 0, \quad (1.8)$$

subject to boundary and initial conditions (1.5), though other variants have also been studied [38]. In (1.8),  $\alpha$  and  $\beta$  are real parameters controlling the anisotropy of the nonlinear and linear terms, respectively. This anisotropic equation was derived by Cuerno & Barabási [14] to describe the nonlinear evolution of surfaces eroded by ion bombardment. It was also studied by Rost & Krug [39] for different combinations of the signs of  $\alpha$  and  $\beta$ . For  $\alpha = \beta > 0$  and  $\mathcal{O}(1)$ , the solutions are bounded and develop into travelling waves that can become oscillatory or chaotic.

In this paper, we provide a comprehensive numerical study of the 2D KSE to complement (and possibly guide) the emerging body of analytical work on this equation. The combination of numerical and analytical studies of the 1D KSE has provided a deep understanding of its solutions and the physical phenomena it describes. It is our goal to extend this tandem approach to the 2D KSE. While there have been a number of numerical studies dedicated to the damped 2D KSE (see for example [40,41] and references therein), a complete numerical study of the 2D KSE (1.4) has not been performed, to the best of our knowledge. In what follows, we study in detail how the solution varies with the domain size by identifying the different attractors and describing their characteristics. We find that many results from the 1D case apply to the 2D equation also, but many others, including the hierarchy of bifurcations, are quite different. In addition, we study the energy of the solution in the chaotic regime. We examine both the dependence of the energy on system size and the dependence of the energy spectrum on wavenumber. We show that equipartition of energy holds in the chaotic regime for the differentiated version of the 2D KSE (see equation (2.4)). We also find that the energy spectrum is radially symmetric in Fourier space and link this property to the  $x - y$  symmetry of the equation.

The structure of this paper is as follows: after introducing the doubly periodic solutions in §2, we study how the energy grows with system size and present results demonstrating the equipartition of energy and extensive dynamics in §3. In §4, we present the linear stability properties of the equation followed by a detailed numerical study for a large range of domain lengths in §5. Finally, the main results and findings of this study are summarized in §6.

## 2. Initial value problem and numerical methods

Throughout this study, we will be considering the initial value problem for the two-dimensional Kuramoto–Sivashinsky equation (1.4) on  $2L_x \times 2L_y$ -periodic domains as given by (1.5). We note that the mean

$$\bar{u}(t) = \frac{1}{4L_x L_y} \int_0^{2L_x} \int_0^{2L_y} u(x, y, t) \, dx \, dy \quad (2.1)$$

of the solution is non-zero and grows in time according to

$$\frac{d}{dt} \bar{u}(t) = -\frac{1}{8L_x L_y} \int_0^{2L_x} \int_0^{2L_y} |\nabla u|^2 \, dx \, dy. \quad (2.2)$$

To focus on the dynamics of the spatially varying part of the solution, we subtract off the growing mean value in our simulations (this is possible since  $\bar{u}(t)$  does not contribute to the dynamics of the higher modes). Therefore, we consider the following mean-zero equation:

$$v_t + \frac{1}{2} \left( |\nabla v|^2 - \frac{1}{4L_x L_y} \int_0^{2L_x} \int_0^{2L_y} |\nabla v|^2 \, dx \, dy \right) + \Delta v + \Delta^2 v = 0 \quad (2.3)$$

for  $v(x, y, t) = u(x, y, t) - \bar{u}(t)$ , subject to the same periodic boundary conditions (1.5). The mean can also be removed by differentiating (1.4) with respect to  $x$  and  $y$  to obtain the system

$$\mathbf{U}_t + (\mathbf{U} \cdot \nabla) \mathbf{U} + \Delta \mathbf{U} + \Delta^2 \mathbf{U} = 0 \quad (2.4)$$

of two mean-zero equations for  $\mathbf{U} = \nabla u$ . This approach has been adopted in many analytical studies [33–36], though for our computations we found using (2.3) to be more straightforward.

With the mean removed, we solve (2.3) subject to the initial condition

$$v(x, y, 0) = \sin\left(\frac{\pi x}{L_x} + \frac{\pi y}{L_y}\right) + \sin\left(\frac{\pi x}{L_x}\right) + \sin\left(\frac{\pi y}{L_y}\right) \quad (2.5)$$

using a Fourier pseudospectral method. This particular choice of initial condition is discussed in §4. The spatial domain  $[0, 2L_x]$  in the  $x$ -direction is split into  $2M_x$  equidistant points and similarly the domain in the  $y$ -direction is discretized using  $2M_y$  points. We express the solution as a Fourier series defined on these grid points and consider the system of ODEs for a finite number of Fourier modes. We compute the nonlinear terms on the grid using fast Fourier transforms to go from Fourier to real space and back again. The time integration of the Fourier modes is carried out using a second-order accurate backwards difference scheme that treats the linear terms implicitly. All codes are home-grown, written in Fortran 95 and compiled using an Intel Fortran compiler. For more details on these numerical methods, see [42,43] for a related two-dimensional equation, and [44] for the dispersive 1D KSE.

In our simulations, we retain  $M_x$  Fourier modes in the  $x$ -direction and  $M_y$  modes in the  $y$ -direction. For the most widely studied case where  $L_x = L_y = L$ , the number of Fourier modes  $M_x = M_y = M$  depends on  $L$  or equivalently  $\nu = \pi^2/L^2$  (see (4.4)). For  $\nu$  between 0.6 and 1.0,  $M = 16$  modes were found to provide sufficient resolution. For the smallest value  $\nu = 0.005$ , however,  $M = 256$  modes were needed. For large values of  $\nu$ , the time step used was  $dt = 5 \times 10^{-3}$  though this was reduced near bifurcation points in order to obtain a sharper estimate of where these occur. We used  $dt = 10^{-4}$  or larger for the smallest values of  $\nu$  in order to accurately capture fast changes in the dynamics. The total time required to enter and characterize an attractor again depends on the value of  $\nu$ . For some chaotic or quasi-periodic cases final times of  $T = 1.5 \times 10^4$  were needed, though typical final times were  $T = 500$  or smaller. Simulations took less than a minute to run for the larger values of  $\nu$ , but took several days and sometimes over a week for small  $\nu$ . All runs used double precision floating point numbers and were run on a 64-bit linux machine with dual Intel Xeon 2.67 GHz CPUs, with six processor cores in each CPU and 16 GB of memory.

### 3. Chaos and energy equipartition

We begin our study by exploring the statistical properties of the solution after it becomes chaotic. As shown later in §4, the long-time solutions of the 2D KSE exhibit spatio-temporal chaos for large values of  $L_x, L_y$ . The rapid oscillations of these solutions suggest a universal bound for both space and time averages of the solutions [27]. We investigate the dependence of the time-averaged energy

$$\langle E(L_x, L_y, t) \rangle = \frac{1}{T_2 - T_1} \int_{T_1}^{T_2} \int_0^{2L_x} \int_0^{2L_y} v^2(x, y, t) dx dy dt \quad (3.1)$$

on domain size as  $L_x, L_y$  become large. Here,  $\langle (\cdot) \rangle = (1/(T_2 - T_1)) \int_{T_1}^{T_2} (\cdot) dt$  denotes time average, and the times  $0 < T_1 < T_2$  are large enough to ensure that the solution has entered the chaotic attractor. As discussed in [28], this quantity for the 1D KSE shares the same scaling with system size  $L$  as  $\limsup_{t \rightarrow \infty} \|u\|_{L_2}$ , and so we adopt (3.1) in order to establish numerically the dependence of  $L_x$  and  $L_y$  on  $\limsup_{t \rightarrow \infty} \|u(\cdot, \cdot; t)\|_{L_2}$ . In the computations described below, the domain size is at least as large as  $30 \times 30$ . We also compute the average energy spectrum (i.e. the power spectrum)

$$S(k_1, k_2) = 4L_x L_y \left\langle |\hat{v}(k_1, k_2, t)|^2 \right\rangle = \frac{1}{T_2 - T_1} \int_{T_1}^{T_2} 4L_x L_y |\hat{v}(k_1, k_2, t)|^2 dt, \quad (3.2)$$

which we normalize by including the factor  $4L_x L_y$ . By examining the power spectrum, we can understand how the energy is divided among different Fourier modes.

For the  $2L$ -periodic 1D KSE, numerical studies have shown that the time-averaged energy density  $\langle E(L, t) \rangle$ , where  $E(L, t) = \|v\|_{L_2}^2$ , is asymptotically proportional to the system size  $L$  [21,29,45]. This suggests that the solution remains  $\mathcal{O}(1)$  and the energy density,  $(1/L)\langle E(L, t) \rangle$ , remains finite for  $L \gg 1$ . The numerically observed upper bound for the  $L_2$ -norm is

$$\limsup_{t \rightarrow \infty} \|v\|_{L_2} \leq cL^{1/2}, \quad (3.3)$$

while the best available analytic bound is  $\mathcal{O}(L^{5/6})$  [28]. Wittenberg & Holmes [29] also show that the time-averaged normalized energy spectrum  $S(k) = 2L \langle |\hat{v}(k, t)|^2 \rangle$  is independent of  $k$  in the region where  $k \ll 1$ . This property is referred to as the equipartition of energy and is in line with the 1D KSE showing extensive dynamics, where a large system is composed of smaller subsystems each exhibiting the same behaviour. To explore how these results might carry over to the 2D KSE, we compute  $\langle E(L_x, L_y, t) \rangle$  and  $S(k_1, k_2)$  for long-time solutions of the 2D KSE for the following three cases:

Case (i):  $L_x = L_y = L$  and  $L \gg 1$

Here we solve the 2D KSE over square domains that increase in size. The time-averaged energy  $\langle E(L, L, t) \rangle$  is plotted against  $L^2$  in figure 1a and shows a linear dependence. A least-squares fit to the data yields a resulting slope of approximately 1.01 so that

$$\langle E(L, L, t) \rangle \sim \text{const. } L^2, \quad L \gg 1. \quad (3.4)$$

Case (ii):  $L_x = 10L_y = 10L$  and  $L \gg 1$

This case is similar to case (i), but the domain is now a rectangle with aspect ratio 10. Though not shown, we obtain a slope of about 0.98 by a least-squares fit to the data. This suggests that  $\langle E(10L, L, t) \rangle = \mathcal{O}(L^2)$ .

Case (iii):  $L_y$  fixed,  $L_x \gg 1$

Here the domain is a rectangle with fixed width  $2L_y = \mathcal{O}(1)$  and increasing length  $2L_x$ . For two fixed values of  $L_y = \sqrt{2}\pi, 2\pi$ , the time-averaged energy is plotted against  $L_x L_y$  in figure 1b. These values of  $L_y$  are chosen to ensure that there are unstable modes in the  $y$ -direction (for large  $L_x$  the domains are thin, but not as thin as the ones studied in [34], in which there were no unstable modes in the  $y$ -direction). Least-squares estimates of the slopes found them to be approximately 1.01 in both cases; hence, when one side of the

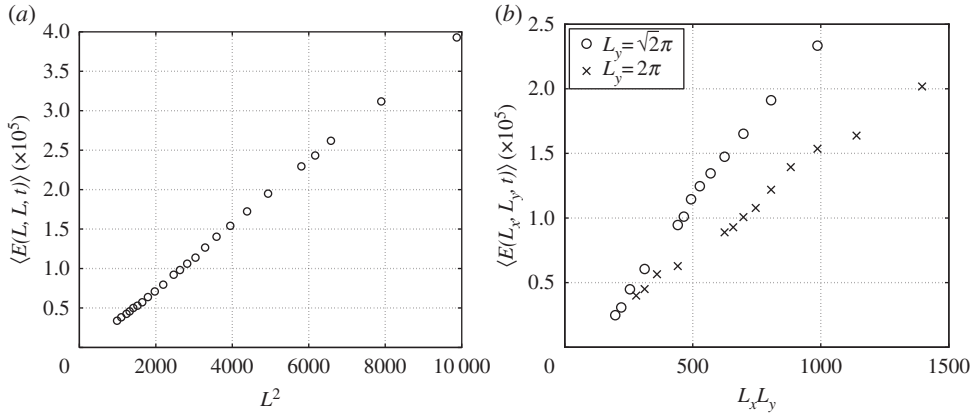


**Figure 1.** Time-averaged energy versus domain area for (a) case (i) ( $L_x = L_y = L$ ) and (b) case (iii) ( $L_y$  fixed). (b) The crosses correspond to the case  $L_y = \sqrt{2}\pi$  while the circles correspond to  $L_y = 2\pi$ .

domain is of fixed length and the other increases, the time-averaged energy scales with the dimension that is varied and produces the same scaling as the 1D KSE.

In addition to the energy, we characterize the average energy spectrum for domains chosen from cases (i) and (ii). The values of  $S(k_1, k_2)$  are shown in figure 2a against

$$k = \sqrt{k_1^2 + k_2^2} = \sqrt{\left(\frac{n_1\pi}{L_x}\right)^2 + \left(\frac{n_2\pi}{L_y}\right)^2}, \quad (3.5)$$

for two different sets of  $(L_x, L_y)$  (here the integers  $1 \leq n_1 \leq M_x$  and  $1 \leq n_2 \leq M_y$  represent the Fourier modes of the two-dimensional solution). It can be seen that the average energy spectra for both sets of  $(L_x, L_y)$  have the same dependence on  $k$ . The independence of the average energy spectrum on domain size is also observed for the 1D KSE [46]. For  $k \ll 1$ , we find that  $S(k_1, k_2) \sim k^{-2}$ , in contrast to a constant value found for the 1D KSE equation (1.1) in [29]. The factor of  $k^{-2}$ , however, is due to the form of the nonlinearity in (2.3) rather than the dimensionality of the problem. To see this, we note that (1.1) is not only (1.4) reduced to one dimension (i.e. equation (1.2)), but also differentiated with respect to  $x$ . The differentiation alters the form of the nonlinear term and yields the additional factor of  $|ik|^2 = k^2$  to the energy spectrum. Note that this  $k^{-2}$  dependence was observed by Yamada & Kuramoto [47] for the integrated equation (1.2).

Considering the differentiated system (2.4), we see that in Fourier space

$$|\widehat{U}_{1k}|^2 = |(\widehat{v}_x)_k|^2 = |ik_1 \widehat{v}_k|^2 = k_1^2 |\widehat{v}_k|^2, \quad |\widehat{U}_{2k}|^2 = |(\widehat{v}_y)_k|^2 = |ik_2 \widehat{v}_k|^2 = k_2^2 |\widehat{v}_k|^2, \quad (3.6)$$

where  $U_1 = v_x$  and  $U_2 = v_y$ . Adding these expressions together gives

$$|\widehat{U}_{1k}|^2 + |\widehat{U}_{2k}|^2 = (k_1^2 + k_2^2) |\widehat{v}_k|^2 = k^2 |\widehat{v}_k|^2. \quad (3.7)$$

Figure 2b shows  $k^2 S(k_1, k_2)$  alongside the sum of the two spectra  $S_1(k_1, k_2) + S_2(k_1, k_2)$ , where  $S_i(k_1, k_2) = \langle |\widehat{U}_{ik}|^2 \rangle$ . Here, we have taken the domain size to be  $L_x = L_y = \pi/\sqrt{0.005}$ . The spectra coincide and the small differences can be attributed to statistical fluctuations in the data.

We further establish that the average energy spectrum for the 2D KSE is a function of the magnitude of the wavenumber,  $k = \sqrt{k_1^2 + k_2^2}$  alone. This can be seen in figures 2 and 3a. We note that this radial symmetry is present even if we have  $L_x \neq L_y$ . To investigate this further, we consider (2.3) in Fourier space and multiply it by  $\widehat{v}_k^*$ , the complex conjugate of  $\widehat{v}_k$ , to obtain

$$\widehat{v}_k^* ((\widehat{v}_k)_t + \frac{1}{2}(|\widehat{\nabla v}|^2)_k - (k^2 - k^4)\widehat{v}_k) = \widehat{c}_0(t), \quad (3.8)$$

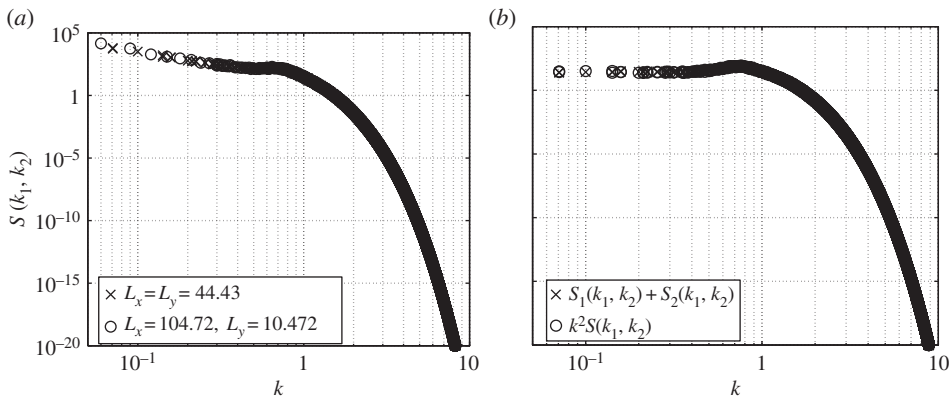


**Figure 2.** (a) The energy spectrum  $S(k_1, k_2)$ , versus  $k$  for  $L_x = L_y = \pi/\sqrt{0.005}$  (crosses), and  $L_x = 10L_y = \pi/\sqrt{0.0009}$  (circles). (b) A comparison between  $k^2 S(k_1, k_2)$  (circles) and  $S_1(k_1, k_2) + S_2(k_1, k_2)$  (crosses) for  $L_x = L_y = \pi/\sqrt{0.005}$ .

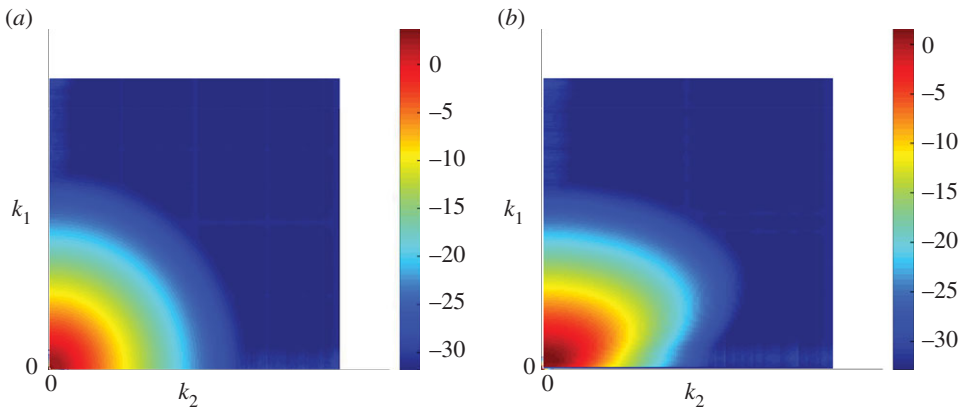


**Figure 3.** Energy spectra from (a) the 2D KSE (2.3) and (b) the asymmetric equation (3.11), both for  $L_x = L_y = \pi/\sqrt{0.01}$ . (Online version in colour.)

where  $\hat{c}_0(t)$  is real and denotes the  $(0,0)$  Fourier coefficient of the integral term  $(1/4L_x L_y) \int_0^{2L_x} \int_0^{2L_y} |\nabla v|^2 dx dy$ . Taking the complex conjugate of (3.8) yields

$$\hat{v}_k((\hat{v}_k^*)_t + \frac{1}{2}(|\widehat{\nabla v}|^2)_k^* - (k^2 - k^4)\hat{v}_k^*) = \hat{c}_0(t). \quad (3.9)$$

Adding (3.8) and (3.9) and averaging in time results in

$$\frac{d}{dt} \langle |\hat{v}_k|^2 \rangle + \langle \hat{v}_k^* (|\widehat{\nabla v}|^2)_k \rangle + \langle \hat{v}_k (|\widehat{\nabla v}|^2)_k^* \rangle - 2(k^2 - k^4) \langle |\hat{v}_k|^2 \rangle = 2 \langle \hat{c}_0 \rangle. \quad (3.10)$$

Since  $d \langle |\hat{v}_k|^2 \rangle / dt = 0$  and the right-hand side is independent of  $k$ ,  $\langle |\hat{v}_k|^2 \rangle$  will be a function of  $k$  only if  $\langle \hat{v}_k^* (|\widehat{\nabla v}|^2)_k + \hat{v}_k (|\widehat{\nabla v}|^2)_k^* \rangle$  depends on  $k$  alone. As a consistency check, we calculated this term numerically and confirmed that indeed it depends only on  $k$ . This analysis suggests that the radial symmetry of the average energy spectrum is tied to the form of the nonlinearity of the 2D KSE, which is symmetric with respect to  $x$  and  $y$ . If we consider instead the following equation:

$$v_t + vv_x + v_{xx} + \Delta^2 v = 0 \quad (3.11)$$

that arises in falling film applications [42,48–50] and lacks symmetry with respect to  $x$  and  $y$ , we find that its energy spectrum is not radially symmetric in  $(k_1, k_2)$ -space; for completeness this is shown in figure 3b, where we have taken  $L_x = L_y = \pi/\sqrt{0.01}$ .



## 4. Domain rescaling and linear stability

Before classifying how the solutions vary with domain size, we first rescale the spatial and time variables according to

$$x \rightarrow \left(\frac{L_x}{\pi}\right)x, \quad y \rightarrow \left(\frac{L_y}{\pi}\right)y \quad \text{and} \quad t \rightarrow \left(\frac{L_x}{\pi}\right)^2 t, \quad (4.1)$$

in order to fix the domain size at  $[0, 2\pi] \times [0, 2\pi]$ . The transformed equation is given by

$$u_t + \frac{1}{2}|\nabla_v u|^2 + \Delta_v u + v_1 \Delta_v^2 u = 0, \quad (4.2)$$

where

$$\nabla_v = \left(\partial_x, \frac{v_2}{v_1} \partial_y\right) \quad \text{and} \quad \Delta_v = \partial_x^2 + \frac{v_2}{v_1} \partial_y^2 \quad (4.3)$$

are the transformed operators and

$$v_1 = \left(\frac{\pi}{L_x}\right)^2 \quad \text{and} \quad v_2 = \left(\frac{\pi}{L_y}\right)^2 \quad (4.4)$$

are bifurcation parameters that play an important role in the dynamics. In rescaling space and time, information regarding the domain size has been transferred to these parameters, which decrease as  $L_x$  and  $L_y$  increase. The corresponding rescaled mean-zero equation for  $v(x, y, t) = u(x, y, t) - \bar{u}(t)$  is

$$v_t + \frac{1}{2} \left( |\nabla_v v|^2 - \frac{1}{4\pi^2} \int_0^{2\pi} \int_0^{2\pi} |\nabla_v v|^2 dx dy \right) + \Delta_v v + v_1 \Delta_v^2 v = 0. \quad (4.5)$$

We assess the linear stability of the uniform state  $v = 0$  and establish the region of instability in  $(v_1, v_2)$  parameter space. Perturbing about the uniform state  $v = 0$ , a normal mode solution is sought in the form

$$v(x, y, t) = \delta(e^{i(n_1 x + n_2 y) + \sigma t} + \text{c.c.}), \quad (4.6)$$

where  $n_1, n_2$  are non-zero integer wavenumbers in the  $x$ - and  $y$ -directions, respectively,  $\delta \ll 1$ ,  $\sigma$  is the complex amplification rate and c.c. denotes complex conjugates. Substituting (4.6) into (4.5) and linearizing with respect to  $\delta$  results in the following dispersion relation:

$$\sigma = \left(n_1^2 + \frac{v_2}{v_1} n_2^2\right) (1 - v_1 n_1^2 - v_2 n_2^2) \quad (4.7)$$

that in turn implies the condition

$$v_1 n_1^2 + v_2 n_2^2 < 1 \quad (4.8)$$

for instability. Inequality (4.8) can be satisfied for sufficiently small  $v_1$  and  $v_2$  (physically this is equivalent to large unscaled domains). By fixing  $v_1$  and  $v_2$ , we can determine the modes  $(n_1, n_2)$  for which the trivial solution is unstable, as summarized in [figure 4](#). We see that, for  $v_1 > 1$  and  $v_2 > 1$ , (4.8) cannot be satisfied for any  $n_1, n_2 \in \mathbb{Z}_+$  and all sufficiently small perturbations from the trivial state decay to zero exponentially fast. If  $v_1$  or  $v_2$  is less than unity, instability sets in. For instance, if initially  $v(x, y, 0) = \sin(x + y)$  so that  $n_1 = 1$  and  $n_2 = 1$ , a positive growth rate is ensured if  $v_1 + v_2 < 1$ . A choice of an initial condition independent of  $y$ , i.e.  $n_2 = 0$ , results in the



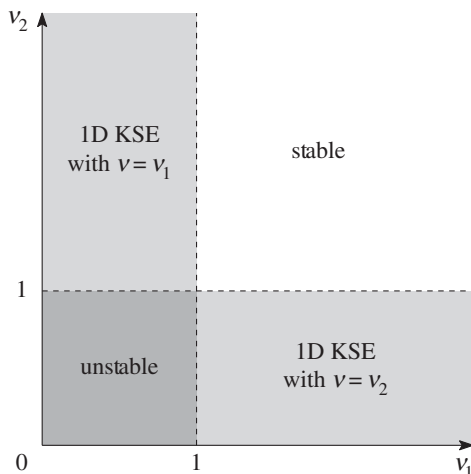


**Figure 4.** Stability diagram for the two-dimensional Kuramoto–Sivashinsky equation. The equation is stable when both  $v_1, v_2 > 1$ . If either  $v_1$  or  $v_2 < 1$ , then the dynamics are described by the 1D KSE. If both  $v_1, v_2 < 1$  then the solutions are fully two-dimensional.

instability condition being independent of  $v_2$  and yields the stability conditions for the 1D KSE (analogous results hold if  $n_1 = 0$ ). Based on the linear stability analysis, we take

$$v(x, y, 0) = \sin(x + y) + \sin(x) + \sin(y) \quad (4.9)$$

as the initial condition in our numerical experiments. This choice gives three initially unstable modes  $(n_1, n_2) = (1, 1), (1, 0), (0, 1)$  that, as we will see later, evolve into solutions with rich dynamical behaviour, including quasi-periodicity and chaos.

## 5. Solutions and their dynamics

Using the numerical method described in §2, we solve the rescaled KSE (4.5) subject to the initial condition (4.9) for a range of  $v_1, v_2$  in the unstable region, namely  $0 < v_1, v_2 \leq 1$  (figure 4). For the 1D KSE, steady-state solutions arise for  $0.3 < v < 1$ , approximately, where  $v = (\pi/L)^2$ , while smaller values of  $v$  result in travelling waves and time-periodic bursts [22,23]. When  $v \leq 0.12115$ , chaotic solutions appear via Feigenbaum subharmonic period-doubling bifurcations [22,23,30]. For the 2D KSE solutions also increase in complexity as  $v_1, v_2 \rightarrow 0$ ; however, there are infinitely many routes to chaotic dynamics depending on the path in  $(v_1, v_2)$  space. We explore the path dependence in detail for two cases,  $v_1 = v_2 = v$  with  $v \rightarrow 0$ , and  $v_2 \rightarrow 0$  with  $v_1$  fixed.

We begin by performing numerical simulations over the unstable range of  $v_1$  and  $v_2$  using step size  $\Delta v = 0.05$  in each direction and classifying the solution at each  $(v_1, v_2)$  point. We exploit the symmetry of the 2D KSE about  $v_1 = v_2$  (under a space and a time-scale transformation) to reduce the number of simulations required: if  $v(x, y, t)$  is the solution corresponding to the values  $(v_1, v_2)$ , then the solution for  $(v_2, v_1)$  is  $v(y, x, (v_2/v_1)t)$ —this can be seen by multiplying the 2D KSE by  $v_1/v_2$ . We identify and study the different attractors by monitoring the energy of the solution

$$E(t) := \|v(\cdot, \cdot, t)\|_{L^2}^2 = \int_0^{2\pi} \int_0^{2\pi} v^2(x, y, t) dx dy. \quad (5.1)$$

This is related to the definition presented in (3.1) for  $2L_x \times 2L_y$ -periodic domains by  $E(t) = \sqrt{v_1} \sqrt{v_2} E(L_x, L_y, t)$ . We also consider

$$\dot{E}(t) = 2\|v_x\|^2 + 2\frac{v_2}{v_1}\|v_y\|^2 - 2v_1\|v_{xx}\|^2 - 4v_2\|v_{xy}\|^2 - 2\frac{v_2^2}{v_1}\|v_{yy}\|^2 - \int_0^{2\pi} \int_0^{2\pi} v \left( v_x^2 + \frac{v_2}{v_1} v_y^2 \right) dx dy, \quad (5.2)$$

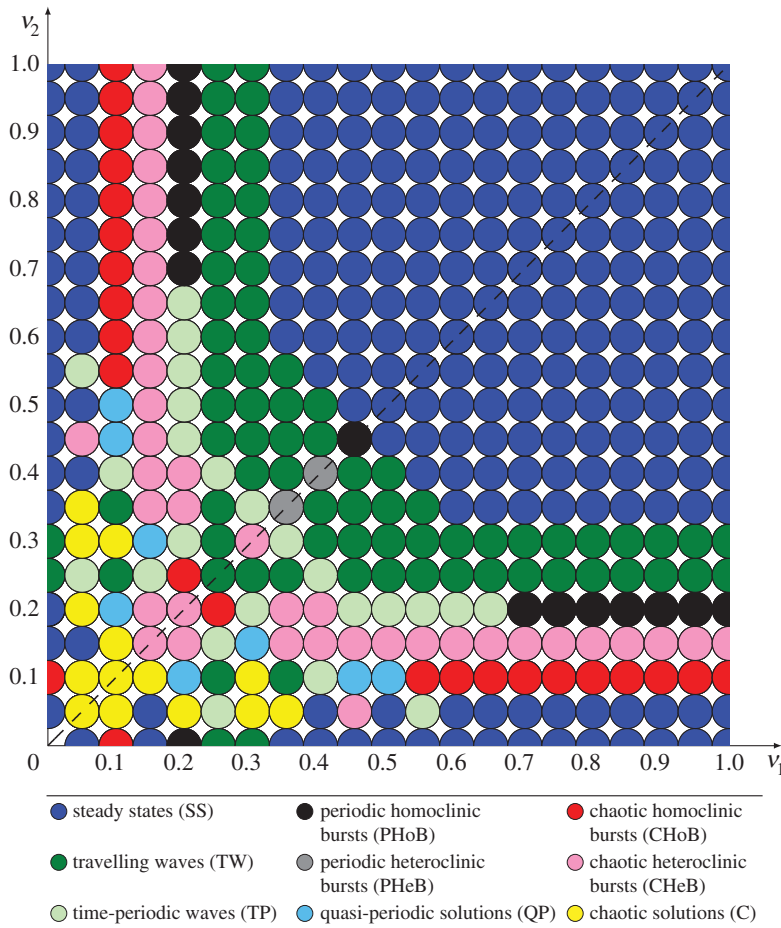


**Figure 5.** Phase diagram classifying the solutions obtained for different values of  $\nu_1$  and  $\nu_2$  for which the KSE is unstable. (Online version in colour.)

which we obtain by multiplying (4.5) by  $v$  and integrating over the periodic domain. Since the solution is periodic, quadratures are performed using the trapezoid rule to compute  $E(t)$  and  $\dot{E}(t)$  to spectral accuracy; these values are in turn used to construct phase-planes  $(E(t), \dot{E}(t))$ , which are particularly useful in identifying periodic and chaotic attractors. We also determine the Poincaré maps where  $\dot{E}(t) = 0$  in order to numerically generate return maps to describe the dynamics [22,23,30,44]. Using second-order polynomial interpolation, we find the times  $t_n$ ,  $n = 1, 2, \dots$ , that give  $\dot{E}(t_n) = 0$ . With  $E_n = E(t_n)$ ,  $n = 1, 2, \dots$ , return maps are constructed by plotting the sequence of points  $(E_n, E_{n+1})$ . The resulting geometric object provides information about the attractor. If the return map contains just one point the solution is time-periodic with a single minimum in the  $E(t)$  signal (the period of oscillation can be estimated by calculating the time difference between two consecutive minima). If the return map contains continuous-looking curves that fill with points as  $n$  increases, the solution is quasi-periodic, while foldings and self-similarity provide strong evidence for chaotic solutions [22,23,30,44,51].

Simulation results from the  $(\nu_1, \nu_2)$  parameter sweep are summarized in the phase diagram in figure 5 with the different solution states indicated by different coloured circles as indicated on the figure. The diagram includes a relatively large region of non-uniform steady states, starting from the bifurcation point  $(\nu_1, \nu_2) = (1, 1)$  and covering almost half of the computational domain. As we decrease the values of  $\nu_1$  and  $\nu_2$ , the steady-state solutions are succeeded by travelling waves or

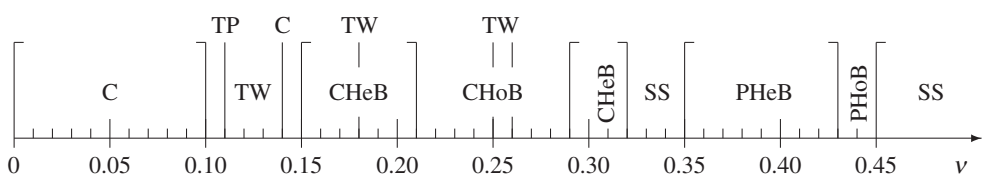


**Figure 6.** Solutions obtained along the line  $\nu_1 = \nu_2 = \nu$  in parameter space. The solution abbreviations are given in the caption of figure 5. The system size increases as we move to the left.

**Table 1.** Solutions for  $0 < \nu_1 \leq 0.35$  and  $\nu_2 < 0.05$ . For comparison, solutions to the 1D KSE for  $0 < \nu \leq 0.35$  are also provided. Most abbreviations are given in the caption of figure 5. We use TP[m] to refer to a time-periodic solution with  $m$  distinct minima in its energy signal.

$\nu_2 \backslash \nu_1$	0.05	0.10	0.15	0.20	0.25	0.30	0.35
0.04	C	C	TP[1]	C	C	C	C
0.03	C	C	QP	C	TP[1]	C	C
0.02	C	C	C	C	TW	TP[3]	C
0.01	C	C	C	C	TP[5]	C	C
0.005	C	C	C	C	TP[1]	C	C
1D KSE $\nu = \nu_1$	SS	CHoB	SS	PHoB	TW	TW	SS

time-periodic waves, including periodic homoclinic bursts and periodic heteroclinic bursts. For relatively small values of  $\nu_1, \nu_2$ , solutions characterized by quasi-periodic or chaotic oscillations in time emerge. Chaotic solutions also appear in the form of chaotic homoclinic bursts or chaotic heteroclinic bursts.

(a) Paths in  $(\nu_1, \nu_2)$ -space

In this section, a more detailed examination is undertaken to determine the dynamics along paths in  $(\nu_1, \nu_2)$ -space as  $\nu_1, \nu_2 \rightarrow 0$ . We first take  $\nu_1 = \nu_2 = \nu$  and compute solutions at equally spaced values of  $\nu$  with step size  $\Delta \nu = 0.01$ . An outline of the most attracting solution types is given in the schematic diagram of figure 6 (note that complexity emerges as we move from right to left). The first solutions to emerge are steady states for parameter values  $0.45 \leq \nu < 1$ . For  $0.43 < \nu < 0.45$ , the fixed point attractor overlaps with a time-periodic attractor, while for smaller values  $0.35 \leq \nu \leq 0.45$ , periodic heteroclinic bursts emerge as the time-periodic attractor competes with a new fixed point attractor. We see the first chaotic solutions for  $\nu$  as high as 0.32. As we let  $\nu \rightarrow 0$ , the solutions alternate between travelling waves and chaotic dynamics until  $\nu = 0.1$ , after which the solutions remain chaotic. This route to chaos was not found to follow the pattern of period doubling bifurcations found in the 1D KSE [22,23]. A notable characteristic of the chaotic solutions is that they retain  $\mathcal{O}(1)$  amplitudes as  $\nu$  decreases but the number of spatial oscillations increase. A similar result holds for the 1D KSE, where it was proved that the number of rapid spatial oscillations increases linearly with the system size [32].

We also investigate the paths  $\nu_2 \rightarrow 0$  for small but fixed  $\nu_1$  between  $0 < \nu_1 \leq 0.35$ . We are particularly interested in seeing whether the 1D KSE solutions  $\nu = \nu_1$  are recovered in this limit—setting  $\nu_2 = 0$  in (4.2) can be seen to yield the 1D KSE with  $\nu = \nu_1$ . The results are summarized in table 1 and it can be seen that, as  $\nu_2$  decreases, solutions are mostly chaotic. Interestingly, our computations do not reduce to the given solution type obtained from the 1D KSE for  $\nu = \nu_1$ , thus suggesting that the limit  $\nu_2 \rightarrow 0$  is singular. In order to observe the quantitative nature of the attractors, two representative return maps are shown in figure 7. Figure 7a corresponds to

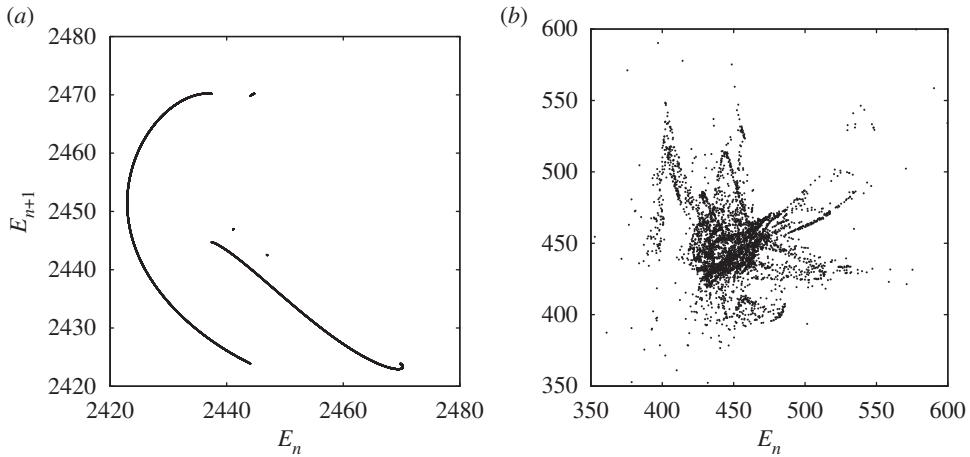


**Figure 7.** Return maps for (a) a quasi-periodic solution ( $\nu_1 = 0.15$ ,  $\nu_2 = 0.03$ ) and (b) a chaotic solution ( $\nu_1 = 0.25$ ,  $\nu_2 = 0.04$ ).

a quasi-periodic solution obtained for  $(\nu_1, \nu_2) = (0.15, 0.03)$ —quasi-periodicity is surmised by the continuous-looking curves. The return map for the solution obtained for  $(\nu_1, \nu_2) = (0.25, 0.04)$  is illustrated in figure 7b, which is surmised to be chaotic due to the presence of foliations.

It can also be seen from figure 5 that steady states emerge when  $\nu_1$  and  $\nu_2$  are relatively close to unity. In what follows we analyse asymptotically the bifurcated steady states emerging from these critical parameter values.

## (b) Steady states

For  $\nu_1 > 1$ ,  $\nu_2 > 1$ , solutions are attracted to the trivial state  $v = 0$ . At  $\nu_1 = \nu_2 = 1$ , a pitchfork bifurcation occurs and non-trivial solutions first appear. In a large region approximately enclosed by the lines  $\nu_1 = 0.35$ ,  $\nu_2 = 0.35$  and  $\nu_1 + \nu_2 = 0.95$  (figure 5), the solutions are two-dimensional unimodal steady states with relatively low energy. A typical steady state for  $\nu_1 = \nu_2 = 0.9$  is given in figure 8a; it is fully two-dimensional and unique up to a translation—equation (4.5) is translation invariant (we do not have a uniqueness proof—our statement is based on numerical experiments starting from arbitrary initial conditions). We can analyse solutions near the bifurcation point  $(\nu_1, \nu_2) = (1, 1)$  by writing

$$\nu_1 = 1 - \alpha_1 \epsilon \quad \text{and} \quad \nu_2 = 1 - \alpha_2 \epsilon \quad (5.3)$$

for  $\alpha_1, \alpha_2 > 0$  and  $0 < \epsilon \ll 1$ . In the analogous 1D analysis, Frisch *et al.* [20] show that the modes  $k = \pm 1$  and  $\pm 2$  alone are relevant to order  $\epsilon$ , and a similar procedure is adopted here to analyse bifurcated steady states of the 2D KSE. We do this by considering the system of equations (2.4) (after transforming it to  $2\pi \times 2\pi$ -periodic domains) and obtaining asymptotic solutions for  $U_1$ ,  $U_2$  as  $\epsilon \rightarrow 0$ . The solutions  $U_1, U_2$  are first expanded in powers of  $\epsilon^{1/2}$  and all the coefficients are written as Fourier series; the coefficients are determined by ensuring that resonant forcing terms vanish at each order, and this process can be carried out to any order. The expression for  $v$  follows from the transformations  $U_1 = u_x = v_x$ ,  $U_2 = u_y = v_y$ . The result is

$$v = 2(12\epsilon)^{1/2} [\alpha_1^{1/2} \cos(x + \phi_1) + \alpha_2^{1/2} \cos(y + \phi_2)] + \epsilon [\alpha_1 \cos(2(x + \phi_1)) + \alpha_2 \cos(2(y + \phi_2))] \\ + 4 \left( \frac{\epsilon}{12} \right)^{3/2} [\alpha_1^{3/2} \cos(3(x + \phi_1)) + \alpha_2^{3/2} \cos(3(y + \phi_2))] + \mathcal{O}(\epsilon^2), \quad (5.4)$$

where  $\phi_1, \phi_2$  are phase shifts in the  $x$ - and  $y$ -directions, respectively, that are present due to translation invariance and can be set to zero without loss of generality. Though not shown, we find good pointwise agreement between the analytical solution (5.4) and that determined numerically.

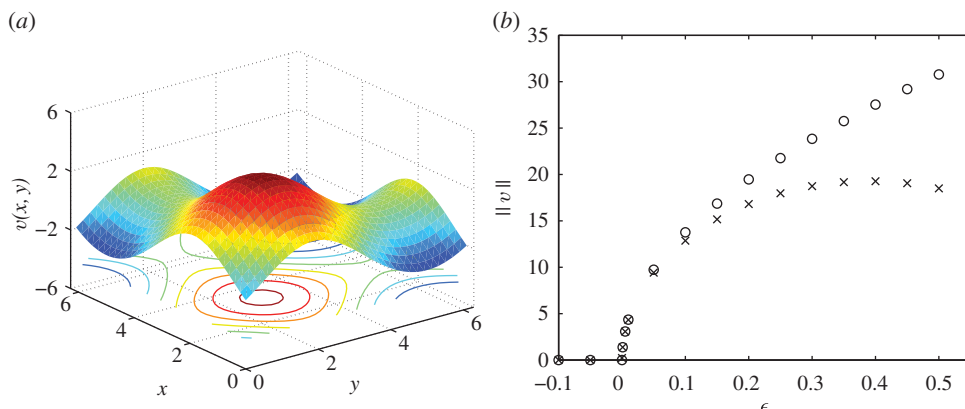


**Figure 8.** (a) Steady-state profile for  $v_1 = v_2 = 0.9$ . (b) The  $L_2$ -norm  $\|v\|$  of steady states for different values of  $\epsilon$  for the numerical (crosses) and analytical (circles) solutions. The analytical norm is found using (5.4) up to order  $\epsilon^{1/2}$ . (Online version in colour.)

Figure 8b shows a bifurcation diagram of the final constant value of  $\|v\|_{L_2}$  against  $\epsilon$  (here  $\alpha_1 = \alpha_2 = 1$ ). The asymptotic solution (5.4) correct to order  $\epsilon^{1/2}$  corresponds to the circular markers while the energy of the numerical solution is indicated by the crosses; agreement is very good for  $\epsilon$  as large as 0.1. As expected, the difference between the two solutions deteriorates as  $\epsilon$  increases. Note also that if  $\epsilon \leq 0$  (i.e.  $v_1 \geq 1$  and  $v_2 \geq 1$ ) the solutions are trivial since  $\limsup_{t \rightarrow \infty} \|v\|_{L_2} = 0$ , and this is the case for both the asymptotic and numerical solutions.

### (c) Travelling waves

As  $v_1$  and  $v_2$  are decreased the steady states described above give way to a travelling wave attractor. It is found that travelling waves are supported for  $v_2 = 0.25, 0.3$  and  $0.55 \leq v_1 \leq 1$  and also in the region  $0.7 \leq v_1 + v_2 \leq 0.9$  (these are depicted in figure 5). The solutions are two-dimensional nonlinear waves of permanent form that travel with constant speed  $c$  in a direction that makes an angle  $\theta$  with the  $y$ -axis, and can be expressed as

$$v(x, y, t) = v(\chi, \psi), \quad \chi = x + ct \sin \theta, \quad \psi = y - ct \cos \theta. \quad (5.5)$$

Substituting (5.5) into (4.5) yields

$$c \sin \theta v_\chi - c \cos \theta v_\psi + \frac{1}{2} \left( v_\chi^2 + \frac{v_2}{v_1} v_\psi^2 \right) + \Delta_{\chi, \psi} v + v_1 \Delta_{\chi, \psi}^2 v = 0, \quad (5.6)$$

where  $\nabla_{\chi, \psi} = (\partial_\chi, (v_2/v_1)\partial_\psi)$  and  $\Delta_{\chi, \psi} = \partial_\chi^2 + (v_2/v_1)\partial_\psi^2$ . Expressions for  $c$  and  $\theta$  that are useful for their numerical determination with spectral accuracy (using Parseval's identities) can be found by multiplying equation (5.6) by  $v_\chi$  and  $v_\psi$ , respectively, and integrating over the domain to provide two equations for  $c$  and  $\theta$ . Solving these yields

$$\theta = \tan^{-1} \left( \frac{A_\chi \int_0^{2\pi} \int_0^{2\pi} v_\psi^2 d\chi d\psi - A_\psi \int_0^{2\pi} \int_0^{2\pi} v_\chi v_\psi d\chi d\psi}{A_\chi \int_0^{2\pi} \int_0^{2\pi} v_\chi v_\psi d\chi d\psi - A_\psi \int_0^{2\pi} \int_0^{2\pi} v_\chi^2 d\chi d\psi} \right), \quad (5.7)$$

where

$$A_\chi = \frac{1}{2} \int_0^{2\pi} \int_0^{2\pi} v_\chi \left( v_\chi^2 + \frac{v_2}{v_1} v_\psi^2 \right) d\chi d\psi, \quad A_\psi = \frac{1}{2} \int_0^{2\pi} \int_0^{2\pi} v_\psi \left( v_\chi^2 + \frac{v_2}{v_1} v_\psi^2 \right) d\chi d\psi \quad (5.8)$$

and

$$c = \frac{A_\chi}{\cos \theta \int_0^{2\pi} \int_0^{2\pi} v_\chi v_\psi d\chi d\psi - \sin \theta \int_0^{2\pi} \int_0^{2\pi} v_\chi^2 d\chi d\psi}. \quad (5.9)$$

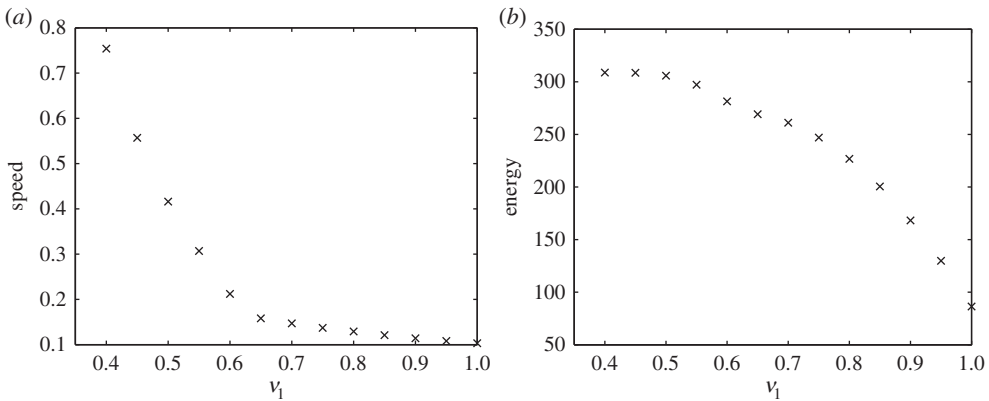


**Figure 9.** Variation of the wave speed  $c$  (a), and energy (b) with  $\nu_1$ , for a fixed value of  $\nu_2 = 0.3$ .

We computed the variation of  $c$  with  $\nu_1$  for the two cases  $\nu_2 = 0.3$  and  $\nu_2 = 0.25$ . In both cases, the speed increases monotonically as  $\nu_1$  decreases, i.e. as the system size in the  $x$ -direction increases. Typical results are depicted in figure 9a for the case  $\nu_2 = 0.3$ . We note that the energy of the travelling waves also changes with  $\nu_1$ , and the variations for the fixed value  $\nu_2 = 0.3$  are given in figure 9b. We also find that this monotonic behaviour with  $\nu_1$  does not persist for all values of  $\nu_2$ . In fact, for  $\nu_2 = 0.25$  the energy increases to a peak value at  $\nu_1 \approx 0.6$ , after which it decreases.

#### (d) Time-periodic solutions

As we decrease the values of  $\nu_1$  and  $\nu_2$  further, we find that various time-periodic solutions emerge. Periodic homoclinic bursts are observed first, and these are found to occur when  $\nu_2 = 0.2$  and  $0.7 \leq \nu_1 \leq 1$ . These solutions can be characterized by their energy evolution consisting of plateaus disrupted by abrupt, though regular, time-periodic bursts. The variation of the period between bursts with  $\nu_1$  and  $\nu_2 = 0.2$  fixed is given in table 2; the periods of oscillation in the range  $0.7 \leq \nu_1 \leq 1$  are given in the first line of the table (lower values of  $\nu_1$  appearing in the second line of the table are discussed below). The results indicate that the period decreases monotonically, albeit rather slowly, from a value of approximately 126.75 at  $\nu_1 = 1$  to 89.9 at  $\nu_1 = 0.7$ . This indicates that the persistence of the steady-state attractor becomes weaker as  $\nu_1$  decreases. An example of these homoclinic burst solutions is given in figure 10 for  $(\nu_1, \nu_2) = (0.8, 0.2)$ . The energy  $E(t)$  and its corresponding phase plane  $(E, \dot{E})$  are shown in Figure 10a,b, respectively; the phase plane is a closed curve that is traversed a single time as the solution evolves over one period in time. The fast bursting dynamics connecting homoclinic states are clearly visible in these numerical results; the solution spends most of its time in the constant energy region and this corresponds to the corner-like part of the phase plane in the vicinity of  $\dot{E} = 0$ . Two characteristic profiles are shown in figure 10c,d, taken from a constant energy state and an energy peak, at times  $t = 360$  and  $t = 381$ , respectively. For these values of  $\nu_1$  and  $\nu_2$ , the steady solutions between bursts are unimodal in  $x$  and bimodal in  $y$ , that is, the only non-zero Fourier modes are  $n_1 \in \mathbb{Z}$  and  $n_2 = 2m_2$ ,  $m_2 \in \mathbb{Z}$ .

Next we consider even lower values of  $\nu_1$ , that is, we fix  $\nu_2 = 0.2$  and study the interval  $0.45 \leq \nu_1 \leq 0.65$ . It is now found that the solutions can be characterized by regular time-periodic oscillations in the energy, as shown in figure 11a corresponding to the particular case  $\nu_1 = 0.5$  and  $\nu_2 = 0.2$ ; the corresponding energy phase plane is depicted in figure 11b. The phase plane is a closed curve confirming periodicity in time, but in addition the presence of the competing steady attractor found for larger values of  $\nu_1$  (figure 10) is no longer felt. The computed periods of oscillation for this range of  $\nu_1$  are given in the second line of table 2. It is evident from these values (and in particular the periods 89.9 at  $\nu_1 = 0.7$  and 2.79 at  $\nu_1 = 0.65$ ) that the time-periodic attractor in  $0.45 \leq \nu_1 \leq 0.65$  is unrelated to that in  $0.7 \leq \nu_1 \leq 1.0$ , in the sense that the transition from the

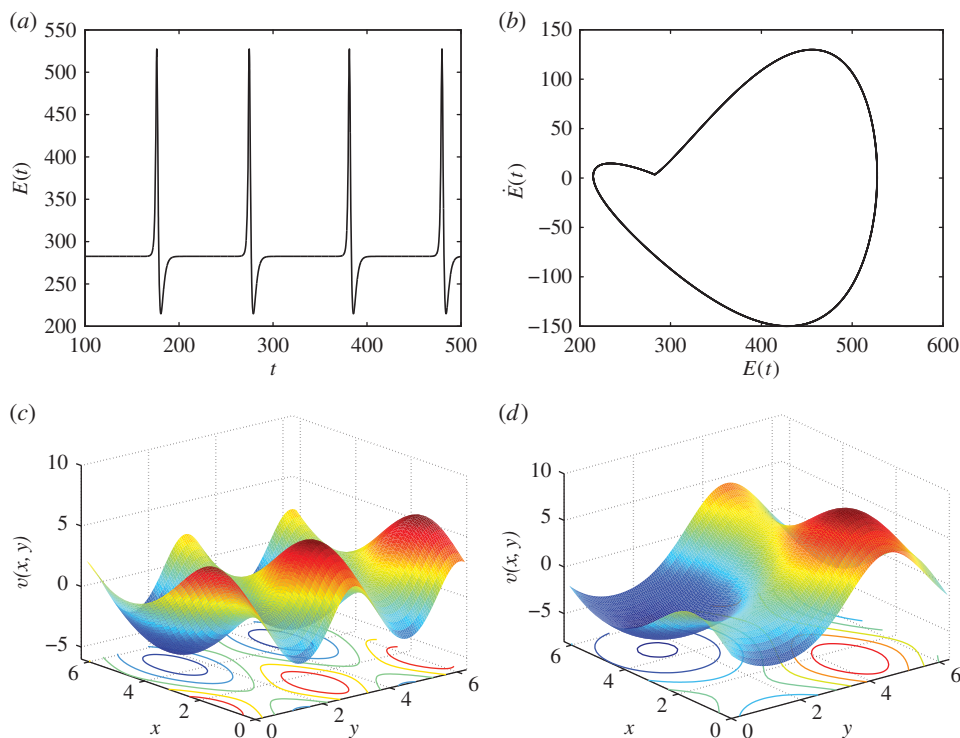


**Figure 10.** Periodic homoclinic burst solutions for  $\nu_1 = 0.8$  and  $\nu_1 = 0.2$ . (a) Evolution of the energy  $E(t)$ ; (b) phase plane of the energy; (c) solution at  $t = 360$  on the constant energy plateau; and (d) solution at  $t = 381$  taken during a burst. (Online version in colour.)

**Table 2.** Oscillation period for time-periodic solutions with  $\nu_2 = 0.2$ . For  $0.7 \leq \nu_1 \leq 1$ , the solutions are periodic homoclinic bursts, while for  $0.45 \leq \nu_1 \leq 0.65$  regular oscillations in the energy signal are observed.

$\nu_1$	1.00	0.95	0.90	0.85	0.80	0.75	0.70
Per	126.75	119	113.5	108.75	102.3	96.15	89.9
$\nu_1$	0.65	0.60	0.55	0.50	0.45	—	—
Per	2.79	2.66	2.57	2.54	2.68	—	—

solution at  $\nu_1 = 0.7$  to that at  $\nu_1 = 0.65$  is not continuous—the solution jumps from one time-periodic attractor to a different one. As with the periodic homoclinic bursts, the period decreases slowly as  $\nu_1$  decreases; however, for the lowest value computed,  $\nu_1 = 0.45$ , the period moves to a slightly higher value. The solutions at  $t = 139$  and again after one and two consecutive periods, respectively, at  $t = 141.54$  and  $t = 144.08$ , are shown in figure 11*c–e*. Interestingly, even though the energy completes one period of oscillation between each profile, we see that the solution requires two complete periods to return to its initial spatial form. This can be understood from the results in figure 11*c–e*. Modulo a constant translation along the line  $x = y$ , the solution in figure 11*d* is identical to those in figure 11*c,e*. This can be seen from the projected contour plots of the solution onto the  $x - y$  plane; in figure 11*c* there is a ‘figure 8’ feature (i.e. a saddle point for the surface) in the middle of the domain, and a rectangular feature (i.e. a local maximum for the surface) in the vicinity of the origin. After one period of oscillation has elapsed the solution is that shown in figure 11*d*, and inspection of the projected contour plot confirms that the saddle and local maximum regions mentioned above are interchanged. This holds for any three solutions



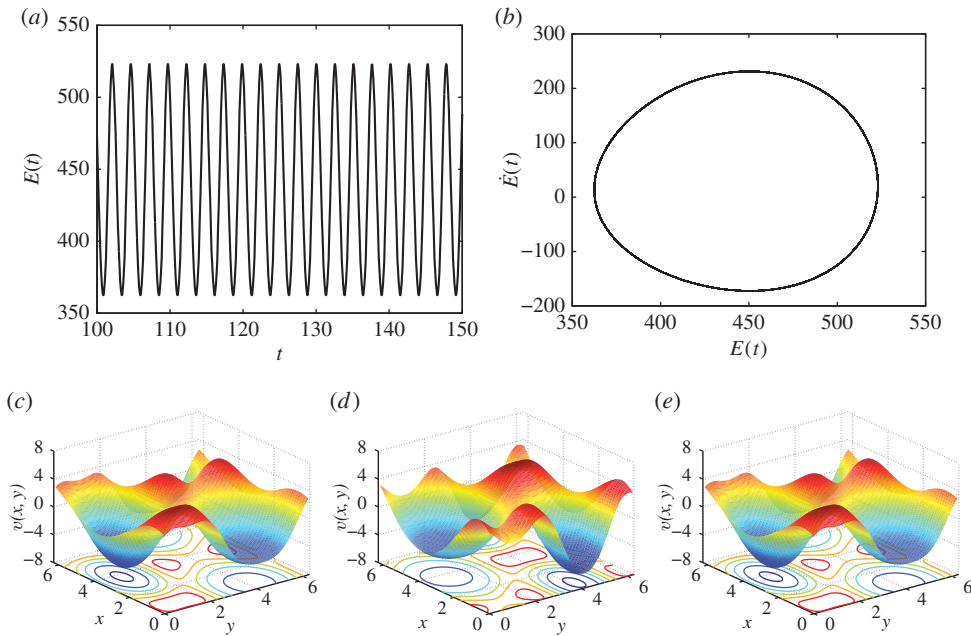


**Figure 11.** (a) Energy, (b) phase plane and solution profiles for the periodic homoclinic solution at  $(\nu_1, \nu_2) = (0.5, 0.2)$ . (c) The solution profile at the minimum energy at  $t = 139$ . (d) The solution one period later ( $t = 141.54$ ) and (e) the solution two periods after (c) ( $t = 144.08$ ). (Online version in colour.)

separated by one period of oscillation between them—we arbitrarily took  $t = 139$  as the first solution in these results—and so the attractor is of travelling periodic type with the solution returning to its initial form modulo a spatial shift, after each period. We find all the solutions on the line  $\nu_2 = 0.2$  have this distinctive feature.

### (e) Quasi-periodicity and chaos

Next we decrease  $\nu_2$  further to the fixed value  $\nu_2 = 0.15$  and vary  $\nu_1$  in the interval  $0.35 \leq \nu_1 \leq 1$ ; we find solutions supporting chaotic heteroclinic bursts along with quasi-periodic and fully chaotic solutions (figure 5). An example of a chaotic heteroclinic burst solution for  $(\nu_1, \nu_2) = (0.85, 0.15)$  is shown in figure 12; the energy evolution given in figure 12a switches between two different fixed points with energy approximately equal to 340 and 300, respectively, and exhibits chaotic bursts in between—this is in contrast to the homoclinic bursts found at larger  $\nu_2$  (figure 10). Evidence of the chaotic nature of the bursts is found in the corresponding energy phase plane (figure 12b), which is composed of non-repeating trajectories. Figure 12(c–e) presents solution profiles at  $t = 1100, 1230, 1300$ , corresponding to times on the higher energy steady-state attractor, during the chaotic burst and at the lower energy steady state, respectively. For the lower energy level ( $t = 1300$ , figure 12e), we find that the profiles are bimodal in  $y$  (i.e.  $y$ -periodic of period  $\pi$ ), but unimodal during the upper energy level (e.g.  $t = 1100$ , figure 12c); during the chaotic bursts the solutions are also unimodal. We emphasize that, for this particular example, only 12 Fourier modes are required in the  $x$ -direction and 30 in the  $y$ -direction to achieve double machine precision. We conclude that, analogously to the 1D KSE [22], complex chaotic solutions exhibit low modal behaviour and can be well characterized by low-order dynamical systems.

As  $\nu_1, \nu_2$  decrease further, complex behaviour persists and includes quasi-periodic oscillations in time (analogous to quasi-periodic flows on a torus with return maps (see §5) consisting of densely filled curves, as in figure 7a). Further decrease of  $\nu_1, \nu_2$  produces large time solutions that are mainly chaotic. This chaotic attractor does not emerge through homoclinic or heteroclinic

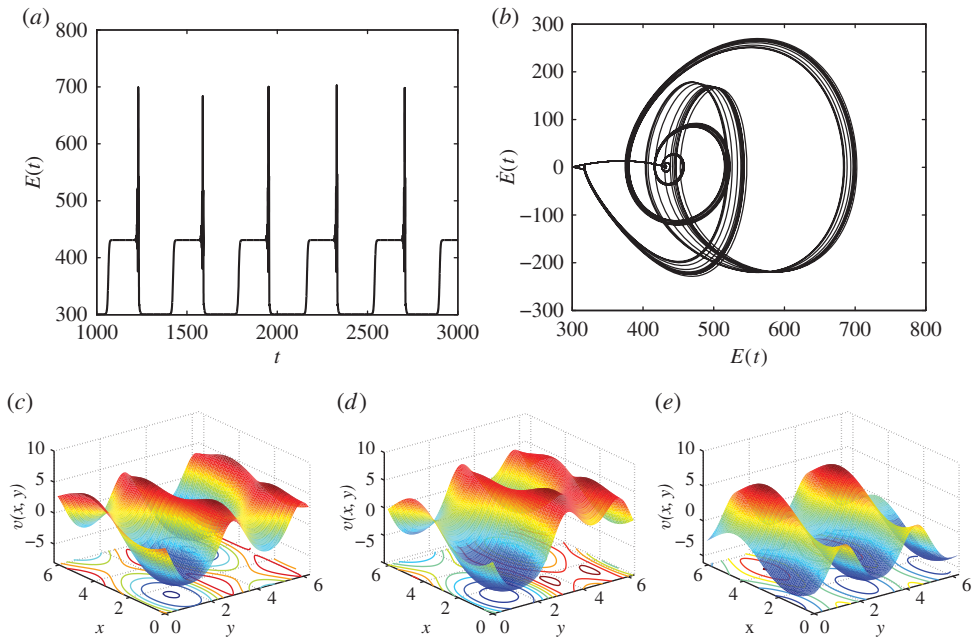


**Figure 12.** (a) Energy, (b) phase plane and solution profiles for the periodic homoclinic solution at  $(v_1, v_2) = (0.85, 0.15)$ . The profiles ((a)  $t = 1100$ , (b)  $t = 1230$ , (c)  $t = 1300$ ) correspond to the solution at the (c) higher energy plateau, during the (d) chaotic burst and at the (e) lower energy plateau. (Online version in colour.)

bursting and assumes a more complicated structure, as seen in the return maps of figure 7b, for example, which exhibit no discernible patterns. Despite this, these solutions can be characterized by their statistical properties, which we have done in §3.

## 6. Conclusion

We presented an extensive numerical study of the 2D KSE equation (1.4), inspired by recent analytical studies [34,35] and encouraged by the success of understanding solution dynamics of the 1D KSE through careful and comprehensive numerical studies. The equation was solved on doubly periodic domains  $[2L_x, 2L_y]$  with particular interest on large domain dynamics. For  $L \gg 1$ , we considered three cases: (i)  $L_x = L_y = L$ ; (ii)  $L_x = 10$ ,  $L_y = 10L$ ; and (iii)  $L_y$  fixed and  $L_x = L$ , with the aim of exploring numerically optimal energy bounds as the system size increases and the solutions become chaotic. Case (iii) is shown to reduce to 1D KSE dynamics, while cases (i) and (ii) produce solutions with energy density asymptotically proportional to the system size (i.e.  $L^2$  in 2D), analogously to the 1D KSE [29]. We linked the long-wave energy spectrum to the form of the nonlinearity in the 2D KSE, showing that it is responsible for both its radial symmetry in Fourier space and its approximate  $k^{-2}$  dependence (figures 2 and 3). Extensive dynamics and the equipartition of energy are recovered by differentiating the solution and considering the energy spectrum of  $U_1 = v_x$  and  $U_2 = v_y$ . This is consistent with efforts [52,53] to model the large-scale chaotic dynamics of the 2D KSE by the Kardar–Parisi–Zhang equation.

We also examined the solutions arising when both  $v_1 = \pi^2/L_x^2 < 1$  and  $v_2 = \pi^2/L_y^2 < 1$ , so that unstable modes are present and the solutions are fully two-dimensional. The  $v_1$ – $v_2$  solution phase space was mapped by solving a large number of initial value problems (figure 5). For values close to the bifurcation point  $v_1 = v_2 = 1$ , we constructed asymptotic solutions that are in good agreement with the computations. As  $v_1, v_2$  decrease these bifurcated solutions become more

nonlinear and unimodal fully 2D steady states emerge. For smaller (but still moderate) values of  $v_1$ ,  $v_2$ , travelling waves and time-periodic solutions emerge, the last appearing in the form of periodic homoclinic or heteroclinic bursts, or solutions with shapes that rapidly oscillate in time—these are similar to those found for the 1D KSE [23]. Solutions evolve to more complicated structures of quasi-periodic or chaotic nature as  $v_1$ ,  $v_2$  decrease sufficiently (equivalently as the domain size increases). These chaotic solutions can arise through an infinite number of paths in  $(v_1, v_2)$ -space, and we explored in detail the paths along  $v_1 = v_2 = \nu \rightarrow 0$ , and  $v_1$  fixed with  $v_2 \rightarrow 0$ . We found that the transition to chaos is via quasi-periodicity and did not observe the pattern of Feigenbaum period-doubling bifurcations found for the 1D KSE [30].

Our computations suggest that the energy bounds of [34,35] in high aspect ratio domains could be extended to more general domain sizes and we suggest an optimal  $L_2$ -bound proportional to the system size (equal to  $L^2$  in our notation). While many of our results show that the 2D KSE and its solutions share features with the 1D KSE, we have also seen differences due to the additional dimension. Perhaps the most notable pertains to transitions to chaos. We have only explored in detail two of the infinitely many paths in  $v_1$ – $v_2$  space, and a closer examination of this aspect of the problem would be interesting. It would also be interesting to explore the effect of dispersion on the 2D KSE by including a term proportional to  $\Delta u_x$  in (1.4). In 1D dispersion can regularize chaotic dynamics into travelling wave pulses [44]. In 2D, there is limited work on equations similar to the differentiated form of the 2D KSE [42,54]; dispersion is found to transform chaotic solutions into travelling wave pulses, but in many cases these travelling waves are unstable in the sense that they do not emerge as solutions to initial value problems. This feature of the 2D problem is quite distinct from that in 1D, where moderate amounts of dispersion produce stable travelling wave pulses. It would be of interest to classify such effects for the 2D KSE.

**Data accessibility.** All data were computed by the authors using their own codes. These can be found at <https://github.com/kalogirou/2D-Kuramoto-Sivashinsky>.

**Authors' contributions.** All authors contributed equally to this work. A.K. carried out the simulations, collected the data and prepared the manuscript. D.T.P. and E.E.K. jointly conceived the study, supervised the analysis of the study and interpretation of data, and edited the manuscript. All authors discussed the results and implications and commented on the manuscript at all stages. All authors gave final approval for publication.

**Competing interests.** There are no competing interests.

**Funding.** The work of D.T.P. was partly supported by EPSRC grant no. EP/K041134/1.

**Acknowledgements.** A.K. acknowledges a Roth Doctoral Fellowship from the Department of Mathematics, Imperial College London.

## References

1. Homsy GM. 1974 Model equations for wavy viscous film flow. In *Nonlinear wave motion*, vol. 15 (ed. AC Newell). Lectures in Applied Mathematics, pp. 191–194. Providence, RI: American Mathematical Society.
2. Nepomnyashchii AA. 1974 Stability of wavy conditions in a film flowing down an inclined plane. {Transl.} *Izv. Akad. Nauk SSSR, Mekh. Zhidk. Gaza* **3**, 28–34.
3. LaQuey RE, Mahajan SM, Rutherford PH, Tang WM. 1975 Nonlinear saturation of the trapped-ion mode. *Phys. Rev. Lett.* **34**, 391–394. (doi:10.1103/PhysRevLett.34.391)
4. Kuramoto Y, Tsuzuki T. 1975 On the formation of dissipative structures in reaction-diffusion systems reductive perturbation approach. *Prog. Theor. Phys.* **54**, 687–699. (doi:10.1143/PTP.54.687)
5. Michelson DM, Sivashinsky GI. 1977 Nonlinear analysis of hydrodynamic instability in laminar flames—I. Derivation of basic equations. *Acta Astronaut.* **4**, 1207–1221. (doi:10.1016/0094-5765(77)90097-2)
6. Sivashinsky GI. 1977 Nonlinear analysis of hydrodynamic instability in laminar flames—I. Derivation of basic equations. *Acta Astronaut.* **4**, 1177–1206. (doi:10.1016/0094-5765(77)90096-0)
7. Sivashinsky GI. 1980 On flame propagation under conditions of stoichiometry. *SIAM J. Appl. Math.* **39**, 67–82. (doi:10.1137/0139007)

8. Papageorgiou DT, Maldarelli C, Rumschitzki DS. 1990 Nonlinear interfacial stability of core–annular film flows. *Phys. Fluids A* **2**, 340–352. (doi:10.1063/1.857784)
9. Tilley BS, Petropoulos PG, Papageorgiou DT. 2001 Dynamics and rupture of planar electrified liquid sheets. *Phys. Fluids* **13**, 3547–3563. (doi:10.1063/1.1416193)
10. Hooper AP, Grimshaw R. 1985 Nonlinear instability at the interface between two viscous fluids. *Phys. Fluids* **28**, 37–45. (doi:10.1063/1.865160)
11. Sivashinsky GI, Michelson DM. 1980 On irregular wavy flow on liquid film down a vertical plane. *Prog. Theor. Phys.* **63**, 2112–2114. (doi:10.1143/PTP.63.2112)
12. Cohen BI, Krommes JA, Tang WM, Rosenbluth MN. 1976 Non-linear saturation of the dissipative trapped ion mode by mode coupling. *Nucl. Fusion* **16**, 971–992. (doi:10.1088/0029-5515/16/6/009)
13. Kuramoto Y, Tsuzuki T. 1976 Persistent propagation of concentration waves in dissipative media far from thermal equilibrium. *Prog. Theoret. Phys.* **55**, 356–369. (doi:10.1143/PTP.55.356)
14. Cuerno R, Barabási A-L. 1995 Dynamic scaling of ion-sputtered surfaces. *Phys. Rev. Lett.* **74**, 4746–4749. (doi:10.1103/PhysRevLett.74.4746)
15. Collet P, Eckmann J-P, Epstein H, Stubbe J. 1993 A global attracting set for the Kuramoto–Sivashinsky equation. *Commun. Math. Phys.* **152**, 203–214. (doi:10.1007/BF02097064)
16. Collet P, Eckmann J-P, Epstein H, Stubbe J. 1993 Analyticity for the Kuramoto–Sivashinsky equation. *Physica D* **67**, 321–326. (doi:10.1016/0167-2789(93)90168-Z)
17. Goodman J. 1994 Stability of the Kuramoto–Sivashinsky and related systems. *Commun. Pure Appl. Math.* **47**, 293–306. (doi:10.1002/cpa.3160470304)
18. Nicolaenko B, Scheurer B, Temam R. 1985 Some global dynamical properties of the Kuramoto–Sivashinsky equations: nonlinear stability and attractors. *Physica D* **16**, 155–183. (doi:10.1016/0167-2789(85)90056-9)
19. Tadmor E. 1986 The well-posedness of the Kuramoto–Sivashinsky equation. *SIAM J. Math. Anal.* **17**, 884–893. (doi:10.1137/0517063)
20. Frisch U, She Z-S, Thual O. 1986 Viscoelastic behaviour of cellular solutions to the Kuramoto–Sivashinsky model. *J. Fluid Mech.* **168**, 221–240. (doi:10.1017/S00222112086000356)
21. Hyman JM, Nicolaenko B, Zaleski S. 1986 Order and complexity in the Kuramoto–Sivashinsky model of weakly turbulent interfaces. *Physica D* **23**, 265–292. (doi:10.1016/0167-2789(86)90136-3)
22. Papageorgiou DT, Smyrlis Y-S. 1991 The route to chaos for the Kuramoto–Sivashinsky equation. *Theor. Comput. Fluid Dyn.* **3**, 15–42. (doi:10.1007/BF00271514)
23. Smyrlis Y-S, Papageorgiou DT. 1996 *Computational study of chaotic and ordered solutions of the Kuramoto–Sivashinsky equation*. Technical report. Hampton, VA: Institute for Computer Applications in Science and Engineering (ICASE).
24. Il'yashenko JS. 1992 Global analysis of the phase portrait for the Kuramoto–Sivashinsky equation. *J. Dyn. Differ. Equ.* **4**, 585–615. (doi:10.1007/BF01048261)
25. Jolly MS, Rosa R, Temam R. 2000 Evaluating the dimension of an inertial manifold for the Kuramoto–Sivashinsky equation. *Adv. Differ. Equ.* **5**, 31–66. (doi:projecteuclid.org/euclid.ade/1356651378)
26. Bronski JR, Gambill TN. 2006 Uncertainty estimates and  $L_2$  bounds for the Kuramoto–Sivashinsky equation. *Nonlinearity* **19**, 2023–2039. (doi:10.1088/0951-7715/19/9/002)
27. Giacomelli L, Otto F. 2005 New bounds for the Kuramoto–Sivashinsky equation. *Commun. Pure Appl. Math.* **58**, 297–318. (doi:10.1002/cpa.20031)
28. Otto F. 2009 Optimal bounds on the Kuramoto–Sivashinsky equation. *J. Funct. Anal.* **257**, 2188–2245. (doi:10.1016/j.jfa.2009.01.034)
29. Wittenberg RW, Holmes P. 1999 Scale and space localization in the Kuramoto–Sivashinsky equation. *Chaos* **9**, 452–465. (doi:10.1063/1.166419)
30. Smyrlis Y-S, Papageorgiou DT. 1991 Predicting chaos for infinite dimensional dynamical systems: the Kuramoto–Sivashinsky equation, a case study. *Proc. Natl Acad. Sci. USA* **88**, 11 129–11 132.
31. Kukavica I. 1994 Oscillations of solutions of the Kuramoto–Sivashinsky equation. *Physica D* **76**, 369–374. (doi:10.1016/0167-2789(94)90045-0)
32. Grujić Z. 2000 Spatial analyticity on the global attractor for the Kuramoto–Sivashinsky equation. *J. Dyn. Differ. Equ.* **12**, 217–228. (doi:10.1023/A:1009002920348)
33. Cao Y, Titi ES. 2006 Trivial stationary solutions to the Kuramoto–Sivashinsky and certain nonlinear elliptic equations. *J. Differ. Equ.* **231**, 755–767. (doi:10.1016/j.jde.2006.08.002)

34. Sell GR, Taboada M. 1992 Local dissipativity and attractors for the Kuramoto–Sivashinsky equation in thin 2D domains. *Nonlin. Anal.* **18**, 671–687. (doi:10.1016/0362-546X(92)90006-Z)
35. Molinet L. 2000 Local dissipativity in  $L^2$  for the Kuramoto–Sivashinsky equation in spatial dimension 2. *J. Dyn. Diff. Equ.* **12**, 533–556. (doi:10.1023/A:1026459527446)
36. Demirkaya A, Stanislavova M. 2010 Long time behavior for radially symmetric solutions of the Kuramoto–Sivashinsky equation. *Dyn. Partial Differ. Equ.* **7**, 161–173. (doi:10.4310/DPDE.2010.v7.n2.a2)
37. Michelson D. 2008 Radial asymptotically periodic solutions of the Kuramoto–Sivashinsky equation. *Physica D* **237**, 351–358. (doi:10.1016/j.physd.2007.09.009)
38. Demirkaya A. 2009 The existence of a global attractor for a Kuramoto–Sivashinsky type equation in 2D. In *Proc. 7th AIMS Int. Conf. on Dynamical Systems and Differential Equations, DCDS Supplement 2009, Arlington, TX, September 2009* (eds X Hou, X Lu, A Miranville, J Su, J Zhu), pp. 198–207. Springfield, MO: American Institute of Mathematical Sciences.
39. Rost M, Krug J. 1995 Anisotropic Kuramoto–Sivashinsky equation for surface growth and erosion. *Phys. Rev. Lett.* **75**, 3894–3897. (doi:10.1103/PhysRevLett.75.3894)
40. Gomez H, Paris J. 2011 Numerical simulation of asymptotic states of the damped Kuramoto–Sivashinsky equation. *Phys. Rev. E* **83**, 046702. (doi:10.1103/PhysRevE.83.046702)
41. Paniconi M, Elder KR. 1997 Stationary, dynamical, and chaotic states of the two-dimensional damped Kuramoto–Sivashinsky equation. *Phys. Rev. E* **56**, 2713–2721. (doi:10.1103/PhysRevE.56.2713)
42. Akrivis G, Kalogirou A, Papageorgiou DT, Smyrlis Y-S. 2015 Linearly implicit schemes for multi-dimensional Kuramoto–Sivashinsky type equations arising in falling film flows. *IMA J. Numer. Anal.* (doi:10.1093/imanum/drv011)
43. Kalogirou A. 2014 Nonlinear dynamics of surfactant-laden multilayer shear flows and related systems. PhD thesis, Imperial College London, UK.
44. Akrivis G, Papageorgiou DT, Smyrlis Y-S. 2012 Computational study of the dispersively modified Kuramoto–Sivashinsky equation. *SIAM J. Sci. Comput.* **34**, A792–A813. (doi:10.1137/100816791)
45. Pomeau Y, Pumir A, Pelce P. 1984 Intrinsic stochasticity with many degrees of freedom. *J. Stat. Phys.* **37**, 39–49. (doi:10.1007/BF01012904)
46. Toh S. 1987 Statistical model with localised structures describing the spatio-temporal chaos of Kuramoto–Sivashinsky equation. *J. Phys. Soc. Jpn* **56**, 949–962. (doi:10.1143/JPSJ.56.949)
47. Yamada T, Kuramoto Y. 1976 A reduced model showing chemical turbulence. *Prog. Theor. Phys.* **56**, 681–683. (doi:10.1143/PTP.56.681)
48. Indireskumar K, Frenkel AL. 1997 Mutually penetrating motion of self-organized two-dimensional patterns of soliton like structures. *Phys. Rev. E* **55**, 1174–1177. (doi:10.1103/PhysRevE.55.1174)
49. Toh S, Iwasaki H, Kawahara T. 1989 Two-dimensionally localized pulses of a nonlinear equation with dissipation and dispersion. *Phys. Rev. A* **40**, 5472–5475. (doi:10.1103/PhysRevA.40.5472)
50. Pinto FC. 1999 Nonlinear stability and dynamical properties for a Kuramoto–Sivashinsky equation in space dimension two. *Discr. Contin. Dyn. Syst.* **5**, 117–136. (doi:10.3934/dcds.1999.5.117)
51. Bergé P, Pomeau Y, Vidal C. 1984 *Order within chaos—towards a deterministic approach to turbulence*. New York, NY: Wiley-Interscience.
52. Jayaprakash C, Hayot F, Pandit R. 1993 Universal properties of the two-dimensional Kuramoto–Sivashinsky equation. *Phys. Rev. Lett.* **71**, 12–15. (doi:10.1103/PhysRevLett.71.12)
53. Boghosian BM, Carson CC, Hwa T. 1999 Hydrodynamics of the Kuramoto–Sivashinsky equation in two dimensions. *Phys. Rev. Lett.* **83**, 5262–5265. (doi:10.1103/PhysRevLett.83.5262)
54. Saprykin S, Demekhin EA, Kalliadasis S. 2005 Two-dimensional wave dynamics in thin films. I. Stationary solitary pulses. *Phys. Fluids* **17**, 1–16. (doi:10.1063/1.2128607)